Medical Engineering and Physics 66 (2019) 56–64

Contents lists available at ScienceDirect

Medical Engineering and Physics

journal homepage: www.elsevier.com/locate/medengphy

Ex vivo validation of microwave thermal ablation simulation using different flow coefficients in the porcine liver

Frank Hübner[a,*], Roland Schreiner[a], Carolin Reimann[b], Babak Bazrafshan[a], Benjamin Kaltenbach[a], Martin Schüßler[b], Rolf Jakoby[b], Thomas Josef Vogl[a]

[a] Institute for Diagnostic and Interventional Radiology, Johann Wolfgang Goethe – University Hospital, Theodor-Stern-Kai 7, 60590 Frankfurt am Main, Germany

[b] Institute for Microwave Engineering and Photonics, Technische Universität Darmstadt, Merckstrasse 25, 64283 Darmstadt, Germany

ARTICLE INFO

Article history:
Received 5 April 2018
Revised 6 February 2019
Accepted 11 February 2019

Keywords:
Microwave thermal ablation
Simulation
Liver tissue
Flow coefficient
Heat distribution

ABSTRACT

The purpose of the study was to validate the simulation model for a microwave thermal ablation in ex vivo liver tissue. The study aims to show that heat transfer due to the flow of tissue water during ablation in ex vivo tissue is not negligible. Ablation experiments were performed in ex vivo porcine liver with microwave powers of 60 W to 100 W. During the procedure, the temperature was recorded in the liver sample at different distances to the applicator using a fiber-optic thermometer. The position of the probes was identified by CT imaging and transferred to the simulation. The simulation of the heat distribution in the liver tissue was carried out with the software CST Studio Suite. The results of the simulation with different flow coefficients were compared with the results of the ablation experiments using the Bland–Altman analysis. The analysis showed that the flow coefficient of 90,000 W/(K*m^3) can be considered as the most suitable value for clinically used powers. The presented simulation model can be used to calculate the temperature distribution for microwave ablation in ex vivo liver tissue.

1. Introduction

Thermal ablation techniques such as radiofrequency ablation (RFA), microwave ablation (MWA) and laser-induced interstitial thermotherapy (LITT) can be used in interventional oncology for the treatment of liver malignancies. The application of hyperthermic energy to destroy tumor cells is based on the denaturation of proteins and the subsequent loss of function leading to cell death. Proteins begin to denature already at about 40 °C, but irreversible coagulation necrosis occurs only from about 60 to 100 °C [1,2].

Microwave coagulation was developed in the early 1980s during hepatic resection in order to achieve hemostasis [3] and has substantially changed the field of thermal ablation in interventional oncology [2]. In oncology, microwave tumor ablation is a minimally invasive treatment for early-stage HCC and oligonodular metastases (three or fewer lesions) and especially for non-resectable liver lesions.

During the treatment, the applicator is positioned percutaneously in the tumor under ultrasound or CT imaging. The emitted electromagnetic energy at the tip of the applicator excites water molecules in the tissue, which results in heat and coagulates the tissue. As the success of the ablation highly depends on the positioning of the applicator tip and the conspicuity of the target tumor, intensive research is currently being conducted on MR-compatible MWA systems. MR-guidance offers appealing characteristics such as excellent soft-tissue resolution, sometimes even without additional use of contrast agent, and the potential of real-time thermosensitive imaging [4].

For the development of these new microwave applicators, experimental tests are carried out in ex vivo tissues in order to evaluate their mode of action and efficiency [4]. Furthermore, theoretical models of the thermal therapy are used for the evaluation. For those models, the Maxwell's equation set as well as the Pennes Bioheat equation is usually applied. The latter includes a term for the heat loss through the microvascular blood perfusion [5]. The heat loss through blood perfusion is often neglected in ex vivo samples because there is no perfusion [6].

However, heating in the microwave ablation leads to partial boiling and evaporation of tissue water. The extracellular and intracellular water flows through destroyed tissue cells and via vessels away from the ablation zone resulting in heat transfer. The flow of water can be clearly observed in MR imaging at high temporal resolution. Therefore, the heat transfer in an ex vivo liver is not negligible.

* Corresponding author.
E-mail address: frank.huebner@kgu.de (F. Hübner).

https://doi.org/10.1016/j.medengphy.2019.02.007
1350-4533/

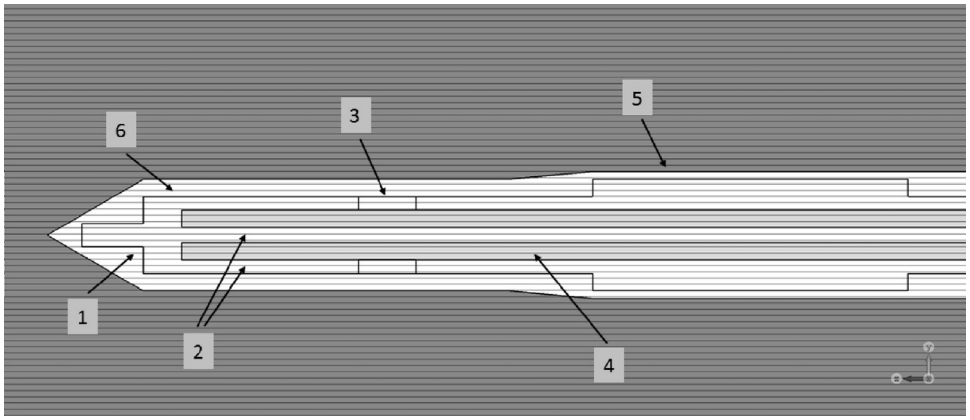

Fig. 1. Design of the coaxial slot antenna with (1) a short-circuited tip, (2) coaxial inner and outer conductor, (3) a slot, (4) dielectric, (5) wave blocker and (6) Teflon.

In this work, the optimal flow coefficient for the simulation of microwave ablation in ex vivo liver tissue is validated. For this purpose experiments are carried out with a commercially available ablation system with different power levels in an ex vivo porcine liver. The temperatures during the heating and the ablation zone induced in the liver are compared with the calculated heat distribution at different flow coefficients.

2. Materials and methods

2.1. Applicator design and simulation

The dimensions of the simulated applicator correspond to a commercially available ablation system (Emprint^{MT} percutaneous antenna, Medtronic, Minneapolis, USA). In the simulation, the applicator is based on a 50 Ω coaxial slot antenna with a short-circuited tip (Fig. 1). The entire outer and inner conductors are made of copper with a small 1.5-mm-wide ring slot in the outer conductor close to the distal tip of the antenna to allow the propagation of electromagnetic waves into the tissue. The coaxial dielectric is a polytetrafluoroethylene (PTFE). The operating resonance frequency of 2.45 GHz is matched with the length of the antenna tip and is controlled by the simulated reflection coefficient. The slot spacing is chosen based on the effective wavelength in liver tissue at the operating frequency, which is calculated using following equation:

$$\lambda_{eff} = \frac{c}{f\sqrt{\varepsilon_r}} \quad (1)$$

where c is the speed of light in free space, f is the operating frequency and ε_r is the relative permittivity of the liver tissue at the operating frequency [6]. The wavelength in liver tissue is therefore 18.5 mm [5]. The slot is placed in a distance of $\lambda_{eff}/4$ from the tip to achieve a stronger electrical field at the output. At a distance of $\lambda_{eff}/2$ from the tip, a cylinder of copper is added on the outer conductor as a wave blocker to mitigate backward traveling waves along the outer shaft of the coaxial cable. It reduces the heating of the cable and further, a more spherical ablation zone is achieved [7,8]. The diameter of the short-circuited tip is reduced to minimize the thickness of the outer shell, thereby increasing the effectiveness of the antenna. The shell is an insulation layer of Teflon which protects the sensitive resonant parts from the high losses caused by the organic tissue.

The simulation of the heat distribution in the liver tissue was carried out with the software CST Studio Suite (Microwave Studio and MPhysics Studio, CST – Computer Simulation Technology, Darmstadt, Germany). The software includes a package for bioelectromagnetic simulation which provides electromagnetic and physiological properties of organic tissues. A bioheat solver (transient thermal solver) is used in the software for the thermal simulation, so that the temperature-dependent tissue parameters, such as the relative permittivity and effective conductivity, vary due to local heating [9,10]. Details of the model used in the simulation are described in the work of Zurbuchen et al. [9].

In the liver model, the default value for the blood flow coefficient is 68,000 W/(K*m^3). But in ex vivo tissue there is usually no blood flow. However, as described in introduction, the heating during the microwave ablation could lead to boiling and evaporation of tissue water. Because of the temperature gradient during ablation, extracellular and intracellular water flows through destroyed tissue cells and via vessels away from the ablation zone. The resulting heat transfer can be described with the flow coefficients. To evaluate this effect, the blood flow coefficient was changed in the software to constant values from 10,000 W/(K*m^3) to 100,000 W/(K*m^3) in 10,000 W/(K*m^3) steps. Thus, for the evaluation a low blood flow coefficient is used, as commonly used in the literature for an ex vivo tissue sample (blood flow is neglected), as well as a blood flow coefficient of 100,000 W/(K*m^3), which is significantly above the default setting for in vivo liver tissue.

In addition, a hexahedral mesh was used which consists of cuboids in the time domain. The length of the cuboids varies throughout the computational volume graded from the smallest to the largest length (pertaining to the smallest and largest mesh cells, respectively). Near to the applicator, a mesh of 30 cells per wavelength was set so that for the smallest cell a size of 0.1 mm and for the largest cell a size of 1.9 mm was calculated (number of cells = 24,485,888). The fine meshing with a size of 0.1 mm around the antenna structure is sufficient for accurate prediction of the radiation pattern at the operating frequency of 2.45 GHz and the resulting 18.5 mm wavelength in liver tissue [5].

2.2. Experimental setup

Microwave ablation was performed in an ex vivo porcine liver using a 15 cm Emprint^{MT} percutaneous antenna (Medtronic, Minneapolis, USA). The applicator was inserted centrally into the liver sample. During the experiments, the temperature was simultaneously recorded by a fiber-optic temperature measurement system (FOTEMP-4, Polytec, Waldbronn, Germany). This system can measure the temperature in a range from −200 °C to +300 °C with an accuracy of up to ±0.2 °C and a resolution of 0.1 °C. Four temperature probes (TS3, Polytec, Waldbronn, Germany), whose measurement points are at the fiber tip, were also positioned in the liver around the applicator (Fig. 2).

The used Emprint^{MT} microwave ablation system allows a maximum adjustable power of 100 W and a maximum ablation time

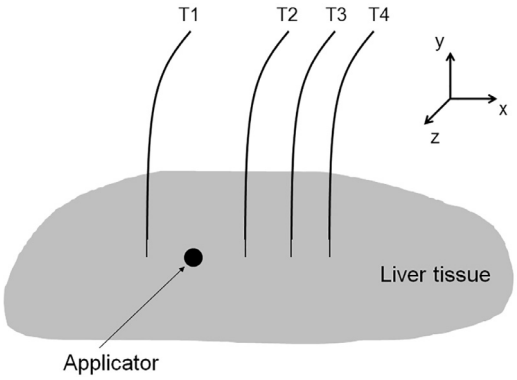

Fig. 2. A schematic of the experimental setup of microwave ablation in an ex vivo porcine liver (transverse plane) using four temperature probes (T1–T4).

Table 1
The positions of the temperature probe tip (T1–T4) related to the applicator tip in each experiment. The position is given in Cartesian coordinates (Fig. 2). The measured temperatures after 10 min of ablation (T_{end}) are presented as well.

Power [W]	Probe	z [mm]	x [mm]	y [mm]	T_{end} [°C]
60	T1	17,2	4,1	2,2	102,6
	T2	14,2	7,2	−1,3	96,7
	T3	14,4	10,3	−1,4	93,5
	T4	14,8	14,5	1,1	70,5
70	T1	4,7	4,5	0,0	84,0
	T2	4,0	4,4	0,0	89,6
	T3	4,1	7,2	0,0	82,2
	T4	2,2	10,9	−1,5	68,8
80	T1	1,3	7,9	0,5	79,9
	T2	2,6	0,4	1,1	125,9
	T3	3,8	4,1	1,3	97,1
	T4	6,8	10,5	1,1	69,9
90	T1	10,0	6,4	0,0	100,8
	T2	14,4	6,2	1,2	100,2
	T3	14,5	8,9	3,3	92,6
	T4	13,6	12,9	1,8	99,3
100	T1	5,2	7,3	1,9	100,2
	T2	8,0	3,0	0,0	101,3
	T3	10,2	6,7	0,0	97,9
	T4	9,6	11,2	1,2	80,2

of 10 min. For this reason, the microwave ablation was applied to the liver sample with powers of 60 W, 70 W, 80 W, 90 W and 100 W for 10 min in order to achieve the largest possible temperature gradient and to evaluate the influence of the flow coefficient. In each experiment, the positions of the probe tips related to the applicator tip were different. In Table 1 this position is given in Cartesian coordinates. The origin of the coordinate system lies at the tip of the applicator. The z-axis is aligned with the applicator axis and the x-axis as well as the y-axis are perpendicular to the applicator (Fig. 2). The exact positions in three-dimensional space were determined by CT imaging (Somatom Definition AS+, Siemens, Healthineers, Erlangen, Germany) and transferred to the simulation. The CT scans (voltage = 120 kVp, effective tube current = 83 mA, pitch = 1) were performed before the ablation (Fig. 3). Transverse and coronal images were reconstructed at 1 mm thicknesses (reconstruction kernel = Siemens H70h).

After the ablation, the applicator was gently removed and the ablation zone in the liver was determined by MR imaging (Magentom Aera, Siemens, Healthineers, Erlangen, Germany) using a turbo spin echo sequence (TR = 700 ms, TE = 12 ms, flip angle = 180°, FOV = 220 × 220 mm^2, matrix = 512 × 512, slice thickness = 2.5 mm) in transverse and coronal planes.

The porcine liver was received from the slaughterhouse shortly before the experiments so that the dehydration of the tissue was minimal. The samples were kept at room temperature at the beginning of the experiments. The initial temperature of each sample was 19.5 °C, 19.5 °C, 19.5 °C, 21.2 °C and 22.0 °C throughout the liver sample.

2.3. Methodology

The used structure of the coaxial slot antenna in the simulation has been validated in previous works [5,6,11,12] and will not be further investigated in this study. However, it is necessary to evaluate the simulation of heat transfer by the resulting flow in an ex vivo tissue sample during ablation. The flow of extracellular and intracellular water caused by the heat is still unknown.

The microwave ablation in the liver tissue was simulated using the flow coefficients specified above, and a heat distribution pattern was created. The temperature was calculated over a period of 10 min at the measurement place of the temperature probes and was compared with the measured temperature. The measured and simulated temperatures were compared using the Bland–Altman analysis [13]. The mean-of-difference (MOD) between the simulated and measured temperatures and the 96% limits-of-agreement (LOA; 1.96 × SD of the differences) were obtained. The flow coefficient with the lowest MOD between simulated and measured temperatures was determined for each temperature probe and microwave power. Subsequently, the optimal flow coefficient was obtained from all experiments and temperature probes by means of the median.

To evaluate the ablation zone, its area observed in the MR images was compared to the area of the calculated temperature map. For this purpose, the 60 °C isothermal area from the simulation was compared with the hypointense region on the MR images. Since the ablation zones typically have an ellipsoidal shape, their maximum radial (d_x) and longitudinal diameter (d_z) were determined and their ellipsoidal area (A) was calculated with $A = \pi/4 * d_x * d_z$.

A differentiation between the dead tissue and the transition zone to the healthy tissue could not be determined exactly, so that a 5% error in the determination of the diameter is assumed. For each flow coefficient and microwave power, the difference between the area observed in the MR images and the isothermal area from the simulation was calculated and then for each flow coefficient the mean deviation was determined.

3. Results

The matching of the coaxial slot antenna was carried out in the liver tissue, since the application of the applicator is also realized in tissue. The CST software calculates the reflection coefficients of the simulated applicator. A comparison of the simulated reflection coefficients of the loaded (in tissue) and unloaded (in air) cases is presented in Fig. 4. The resonance frequency shift between both cases is 3.44 GHz.

With the described applicator structure and matching, a microwave ablation with different flow coefficients in the liver tissue was simulated. As an example, the simulated and measured temperatures of five experiments are presented in Fig. 5(a)–(e). A large range of simulated temperatures depending on the flow coefficient is shown. The influence of the coefficient on the simulation results is obvious.

The correlation analysis of the measured and calculated temperatures for all measurement points and powers reveals the highest correlation at the flow of 10,000 W/(K*m^3) and 20,000 W/(K*m^3) (correlation coefficient between 0.9907 to 0.9993; median = 0.9931). However, the correlation coefficient merely describes the correlation of the curves to each other.

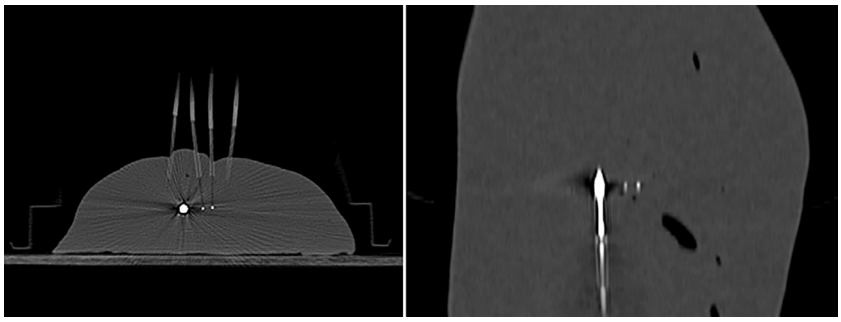

Fig. 3. CT imaging to determine the positions of the temperature probe tips in transverse (left) and coronal (right) orientation.

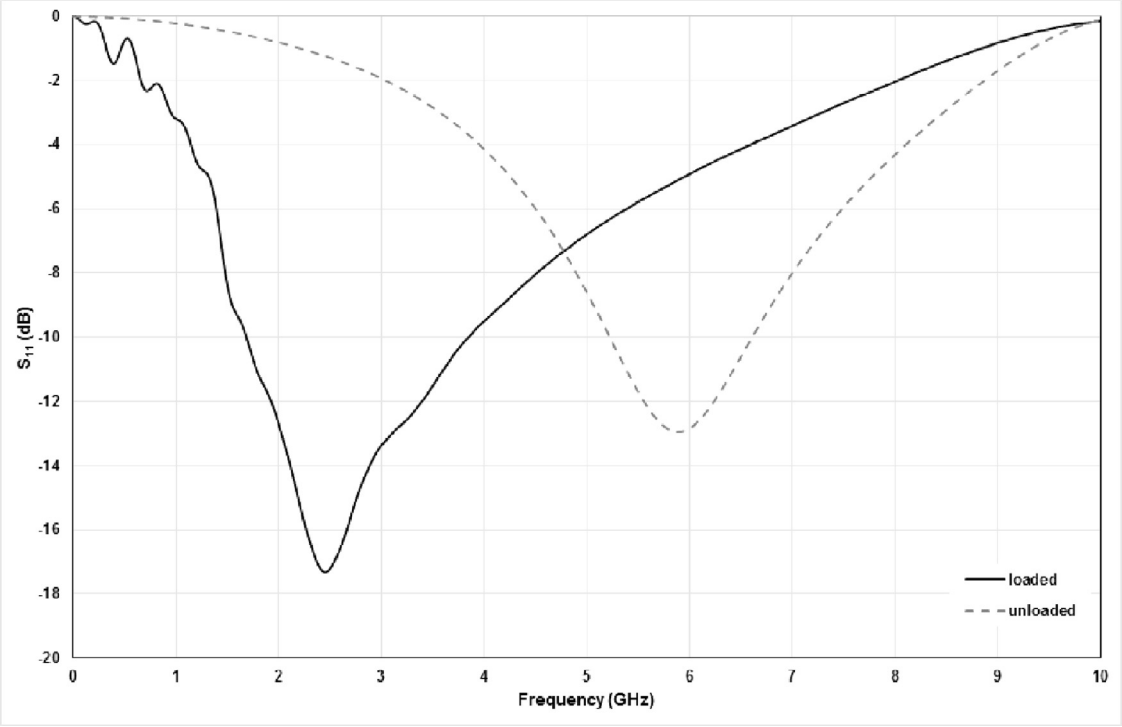

Fig. 4. The simulated reflection coefficient of the loaded (solid line) and unloaded (dashed line) coaxial slot antenna.

Looking at the absolute temperature values, a large difference between the measured and simulated values can be seen at low flow coefficient (Fig. 5(a)–(e)).

For this reason, the Bland–Altman analysis was used to quantify the discrepancy between measured and simulated temperature [13]. As an example, Fig. 6 demonstrates the Bland–Altman plot regarding the experiment at 90 W with the probe T2 and a flow coefficient of 80,000 W/(K*m^3). The average of measured and simulated temperature is shown on the *X*-axis, while the *Y*-axis shows the temperature deviation and the MOD. Furthermore, the MOD and LOA of each experiment are listed in Table 2.

In comparison to the correlation coefficient, the Bland–Altman method shows a greater agreement at higher flow coefficients, since the respective MOD is lower. The results of the experiment with a power of 60 W are an exception and give the best agreement at 30,000 W/(K*m^3), 40,000 W/(K*m^3), and 50,000 W/(K*m^3). Table 3 lists for each experiment the flow coefficient related to the lowest MOD. Hence, the flow coefficient of 80,000 W/(K*m^3) can be considered as the most suitable value for the simulation using the median. If the experiments at the power of 60 W are not considered for the calculation due to their significant deviation from the other results, the flow coefficient of 90,000 W/(K*m^3) will be more suitable.

Furthermore, the area of the ablation zone obtained from MR images was evaluated with the 60 °C isothermal area calculated through the simulation. The lowest average deviation between the determined areas can be observed at a flow coefficient of 50,000 W/(K*m^3). The mean deviation at 50,000 W/(K*m^3) is 40.3 mm^2 (Table 4). Differentiation between the dead tissue and the transition zone to the healthy tissue could not be exactly determined on the MR image without contrast agent. Further, the effect of the tissue shrinkage was not considered in the evaluation [14,15,16,17].

4. Discussion

To validate the simulation of microwave ablation in the ex vivo liver tissue, the dimensions of a commercial ablation system were adopted in the design of the simulated applicator. Microwave applicators are used for minimally invasive ablation therapies. Therefore, the applicator design is made as a needle-like surgical tool for an optimal positioning of the sensor in the organ. In this work, it was decided therefore for a coaxial slot antenna whose structure is known in the literature [5,6,11].

Regarding the shape of the heating area, there is a good agreement between the simulation and the commercial ablation system

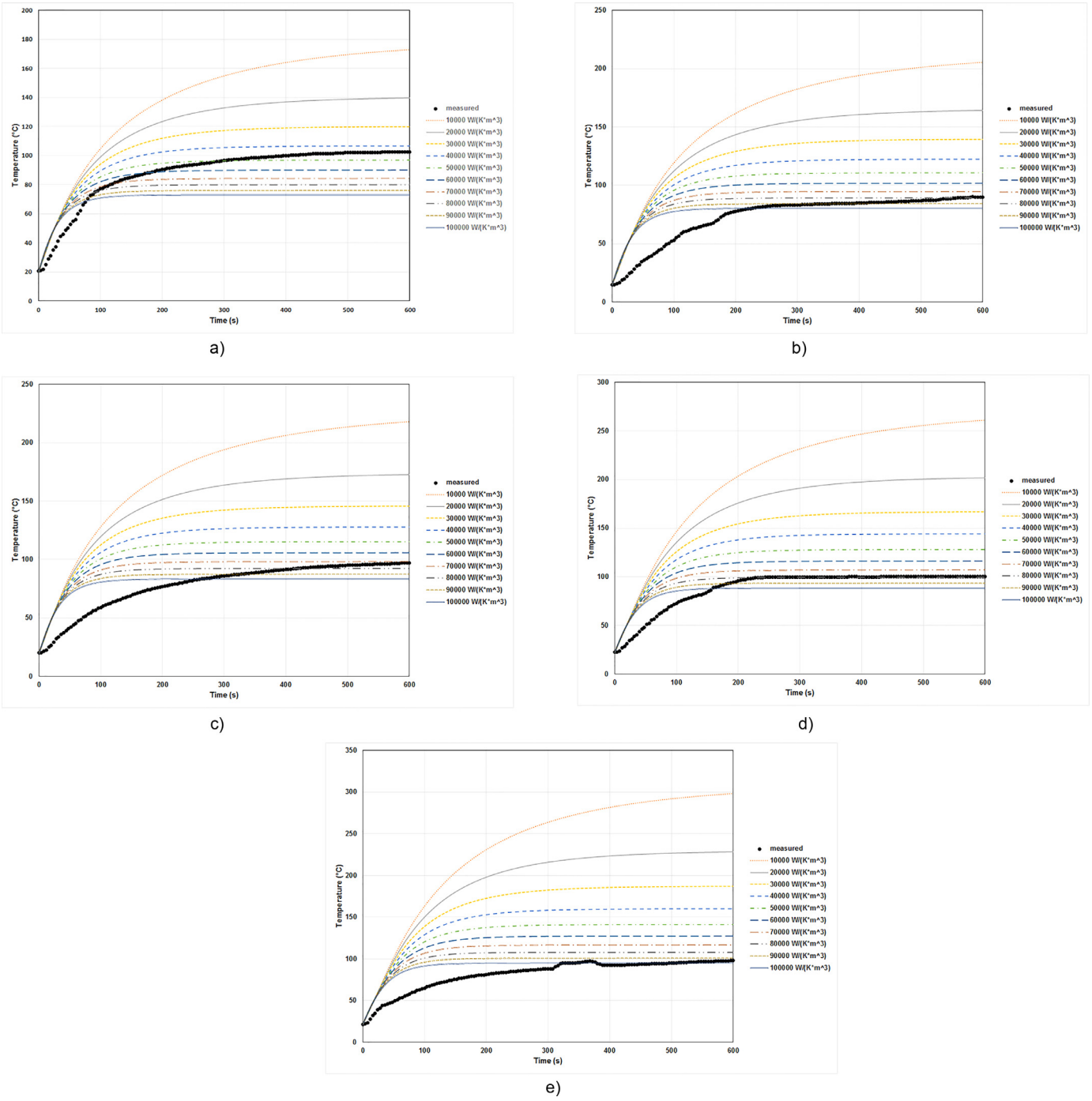

Fig. 5. (a)–(e) The measured (dots) and simulated (lines) temperatures related to the experiments at (a) 60 W and probe 1, (b) 70 W and probe 2, (c) 80 W and probe 3, (d) 90 W and probe 2 and (e) 100 W and probe 3.

used in the experiments of this study (Figs. 7 and 8). The frequency shift between the unloaded and loaded antenna can be attributed to the high capacitive effect of the liver [18,19]. Accordingly, the matching of the antenna in the liver is crucial for a comparability of the simulated heat distribution with a real ablation, as has been done successfully at 2.45 GHz here.

For comparison, microwave ablation was applied to an ex vivo porcine liver sample by means of a microwave applicator, which is also clinically used in patient hyperthermic treatments. In the experiments, a high-resolution CT image reconstruction in two planes was performed to identify the positions of the applicator and temperature probes. Since the CT imaging was carried out before heating, the effect of tissue shrinkage and thus the shift of the probe positions was neglected in this work. Caused by dehydration and thermal tissue destruction in the liver ablation, the tissue volume can shrink between 22% and 74% [14,15,20,21,22]. Most recent studies carried out under CT imaging indicate a volumetric contraction of 40–50% for ex vivo MW ablation [16,17,23]. In this setup, the shrinkage rates could not be determined and integrated into the simulation. Because of the shrinkage effect, the temperature probes could move closer to the applicator over time. The study by Lui and Brake describes the contraction of liver tissue and the displacement of fiber optic temperature probes (and aluminum markers) during microwave ablation [16]. It should be considered

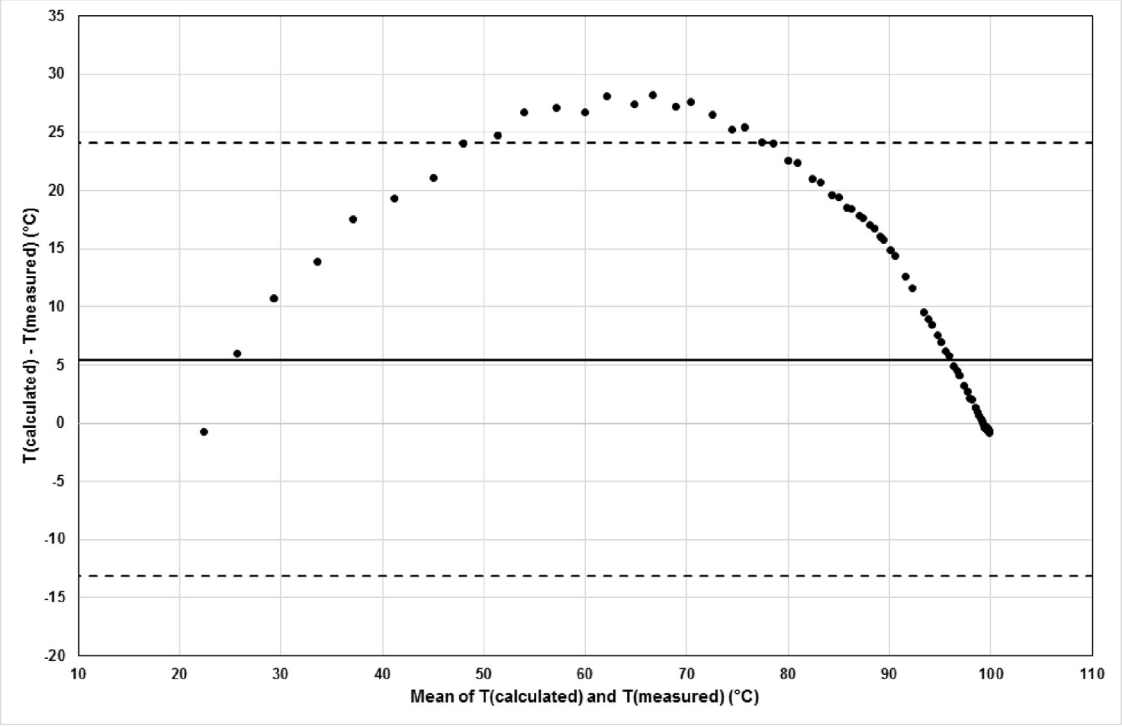

Fig. 6. Bland–Altman plot comparing the measured (probe 2) with the calculated (at flow coefficient of 80,000 W/(K*m^3)) temperatures of the experiment performed with a power of 90 W. The mean-of-difference and the 96%-limits-of-agreement are presented and were assessed as 5.5 ± 18.6 °C.

Table 2
Results of the Bland-Altman analysis of all experiments and probes with different flow coefficients. The mean-of-difference and the 96%-limits-of-agreement of the temperatures are presented.

		Flow coefficient [W/(K*m^3)]									
		10,000	20,000	30,000	40,000	50,000	60,000	70,000	80,000	90,000	100,000
Power [W]	Probe	Mean-of-differences (96%-limits-of-agreement) [°C]									
60	T1	51.1 (±36.2)	31.8 (±16.1)	18.5 (±6.0)	8.9 (±7.8)	1.7 (±12.5)	4.0 (±16.3)	8.6 (±19.3)	12.4 (±21.7)	15.5 (±23.6)	18.2 (±25.2)
	T2	50.6 (±40.4)	29.9 (±16.8)	16.0 (±5.2)	6.3 (±8.9)	1.0 (±14.6)	6.5 (±18.9)	10.9 (±22.2)	14.4 (±24.7)	17.3 (±26.8)	19.7 (±28.4)
	T3	24.8 (±13.2)	10.5 (±9.8)	1.4 (±19.7)	4.8 (±26.3)	9.2 (±30.7)	12.5 (±33.7)	15.1 (35.9)	17.1 (±37.5)	18.7 (±38.8)	20.0 (±39.8)
	T4	13.1 (±6.0)	6.5 (±12.3)	2.5 (±18.3)	0.1 (±22.1)	2.0 (±24.5)	3.3 (±26.1)	4.2 (±27.3)	5.0 (±28.1)	5.6 (±28.8)	6.1 (±29.3)
70	T1	90.0 (±57.2)	67.6 (±35.7)	52.3 (±24.2)	41.1 (±18.6)	32.7 (±16.6)	26.1 (±16.4)	20.8 (±17.2)	16.4 (±18.2)	12.7 (±19.2)	9.6 (±20.1)
	T2	89.8 (±54.0)	66.0 (±30.1)	49.5 (±17.7)	37.5 (±13.5)	28.4 (±14.5)	21.2 (±17.0)	15.5 (±19.6)	10.8 (±21.9)	6.8 (±23.7)	3.4 (±25.3)
	T3	54.8 (±34.7)	36.8 (±18.5)	24.9 (±17.1)	16.6 (±20.7)	10.6 (±24.3)	6.0 (±27.1)	2.4 (±29.3)	0.4 (±31.0)	2.7 (±32.3)	4.6 (±33.3)
	T4	23.1 (±14.9)	15.0 (±13.8)	9.9 (±18.7)	6.4 (±22.5)	4.1 (±25.0)	2.4 (±26.8)	1.1 (±28.1)	0.2 (±29.1)	0.6 (±29.8)	1.2 (±30.4)
80	T1	38.7 (±25.0)	24.0 (±15.4)	14.8 (±18.5)	8.6 (±22.7)	4.2 (±25.9)	1.0 (±28.1)	1.4 (±29.7	3.3 (±31.0)	4.8 (±31.9)	5.7 (±32.6)
	T2	63.9 (±33.9)	45.1 (±18.9)	32.0 (±13.8)	22.2 (±14.3)	14.7 (±16.6)	8.6 (±19.0)	3.6 (±21.1)	0.6 (±23.0)	4.3 (±24.5)	7.8 (±25.7)
	T3	95.6 (±57.3)	69.0 (±32.1)	50.9 (±19.9)	37.9 (±16.0)	28.1 (±16.7)	20.4 (±18.9)	14.2 (±21.2)	9.2 (±23.2)	4.9 (±24.9)	1.6 (±26.3)
	T4	55.3 (±40.3)	37.4 (±20.6)	26.2 (±14.3)	18.6 (±14.9)	13.3 (±17.1)	9.4 (±19.2)	6.4 (±20.8)	4.1 (±22.1)	2.2 (±23.1)	1.1 (±23.9)
90	T1	138.5 (±90.2)	99.8 (±53.7)	73.9 (±34.2)	55.5 (±24.4)	41.8 (±20.7)	31.2 (±20.6)	22.8 (±21.9)	15.9 (±23.6)	10.2 (25.3)	5.4 (±26.8)
	T2	117.5 (±82.3)	82.0 (±46.1)	58.3 (±25.6)	41.5 (±14.3)	29.0 (±10.5)	19.4 (±12.4)	11.7 (±15.6)	5.5 (±18.6)	0.3 (±21.2)	4.1 (±23.3)
	T3	70.9 (±51.1)	44.6 (±22.9)	27.9 (±13.4)	16.6 (±15.8)	8.5 (±20.3)	2.5 (±23.9)	2.1 (±26.7)	5.8 (±28.8)	8.8 (±30.5)	11.3 (±31.8)
	T4	16.4 (±19.1)	0.2 (±17.3)	10.3 (±27.5)	16.8 (±34.5)	21.4 (±39.1)	24.6 (±42.3)	27.1 (±44.6)	29.0 (±46.2)	30.5 (±47.5)	31.8 (±48.5)
100	T1	86.7 (±65.7)	55.4 (±31.7)	35.3 (±15.0)	21.4 (±11.5)	11.4 (±15.5)	3.8 (±19.8)	2.0 (±23.4)	6.7 (±26.2)	10.5 (±28.4)	13.7 (±30.2)
	T2	253.4 (±135.1)	205.9 (±95.6)	172.4 (±71.9)	147.4 (±56.1)	127.9 (±45.1)	112.1 (±37.2)	99.1 (±31.4)	88.0 (±27.1)	78.6 (±23.8)	70.4 (±21.5)
	T3	152.1 (±105.8)	110.0 (±64.2)	82.0 (±40.9)	62.2 (±27.2)	47.5 (±19.7)	36.2 (±16.5)	27.2 (±16.2)	19.9 (±17.3)	13.9 (±18.8)	8.8 (±20.3)
	T4	69.0 (±51.7)	45.0 (±24.6)	30.1 (±14.8)	20.3 (±15.3)	13.4 (±18.3)	8.3 (±21.1)	4.5 (±23.3)	1.5 (±25.0)	1.0 (±26.3)	2.9 (±27.3)

Table 3
Flow coefficients at which the lowest mean-of-difference between simulated and measured temperatures were calculated through the Bland–Altman analysis.

Power [W]	Flow coefficient [W/(K*m^3)]			
	T1	T2	T3	T4
60	50,000	50,000	30,000	40,000
70	100,000	100,000	80,000	80,000
80	60,000	80,000	100,000	100,000
90	100,000	90,000	70,000	20,000
100	70,000	100,000	100,000	90,000

in the evaluation as a source for a potential systemic error towards higher temperatures.

On the other hand, looking at the calculated temperature curves over the ablation time, it is striking that the temperature values are enormously high at low flow coefficients. Disregarding the heat transfer by the water flow completely, the temperatures would be even higher. The measured temperatures reached in all experiments a maximum value of 125.9 °C (Table 1). The results showed that there is a higher correlation between the measured and calculated temperature values at high flow coefficients (Fig. 5(b)–(e)).

Table 4
Comparison of the ablation zone area observed on the MR images with the area of the 60 °C isotherm determined by the simulation at different flow coefficients. The mean deviation is determined for each flow coefficient.

		Flow coefficient [W/(K*m³)]									
		10,000	20,000	30,000	40,000	50,000	60,000	70,000	80,000	90,000	100,000
Power [W]	MRI [mm²]	Simulation [mm²]									
60	501.1 (−48.9 to 51.4)	1213.0	929.4	748.4	630.7	549.7	494.0	449.6	408.4	373.9	350.2
70	602.9 (−58.8 to 61.8)	1313.7	1029.2	827.0	706.3	607.7	549.9	503.8	463.0	423.5	398.7
80	725.0 (−70.7 to 74.3)	1496.7	1150.8	931.2	791.7	684.8	610.6	556.5	507.8	475.4	441.8
90	819.6 (−79.9 to 84.0)	1605.3	1271.3	1010.6	848.8	743.8	656.3	601.2	555.7	518.7	480.9
100	839.9 (−81.9 to 86.1)	1686.4	1349.2	1090.8	928.6	807.8	726.2	647.2	597.6	552.0	517.8
		Difference [mm²]									
60		711.9	428.3	247.3	129.6	48.6	7.0	51.4	92.6	127.1	150.9
70		710.8	426.3	224.1	103.4	4.8	53.0	99.1	139.9	179.4	204.2
80		771.7	425.8	206.3	66.7	40.2	114.4	168.4	217.1	249.6	283.1
90		785.6	451.7	190.9	29.2	75.9	163.4	218.4	263.9	301.0	338.8
100		846.5	509.2	250.9	88.7	32.1	113.8	192.7	242.3	288.0	322.1
Mean deviation [mm²]:		765.3	448.3	223.9	83.5	40.3	90.3	146.0	191.2	229.0	259.8

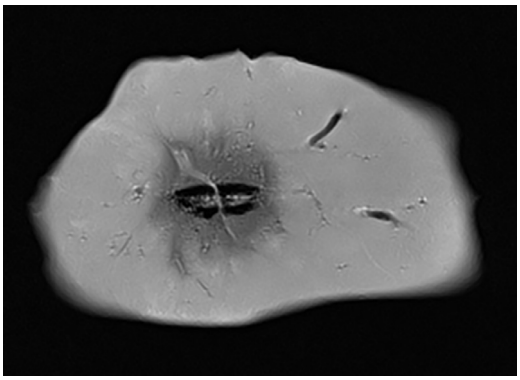

Fig. 7. MR imaging of the porcine liver sample after microwave heating with a power of 90 W. The ablated area is hypointense compared to the rest of the liver.

An exception appears in the experiment with the low power of 60 W (Fig. 5(a)). Bland–Altman evaluation of the flow coefficient yielded a median of 80,000 W/(K*m³) for all experiments. At low powers, the thermal destruction of the tissue over time is less, so that the resulting tissue water flow is lower than at higher power levels. The influence of the heat transfer on the temperature distribution seems to be lower. For this reason, for low power levels (<70 W) and small ablation zones, further evaluations are required to determine the temperature distribution. For large tumors, higher powers up to 100 W are used in the clinical application with the used microwave ablation system [24,25,26]. This results in higher temperature gradients causing a larger flow coefficient. Considering only the results of the powers from 70 W to 100 W, a median flow coefficient of 90,000 W/(K*m³) would be optimal.

Fig. 7 shows the effects of hot water flowing through the vessels away from the ablation zone and forming small satellites with coagulated tissue. The heat transfer through the resulting flow in an ex vivo liver tissue is therefore not negligible.

However, the evaluation of the calculated ellipsoidal area of the ablation zone between the MR image and the simulation revealed a higher correlation with a flow coefficient of 50,000 W/(K*m³). The area of the hypointense region in the MR image (Fig. 7) was compared with the area of the 60 °C temperature zone of the calculated temperature distribution under different flow coefficients (Fig. 8). In the hypointense region, it is difficult to differentiate

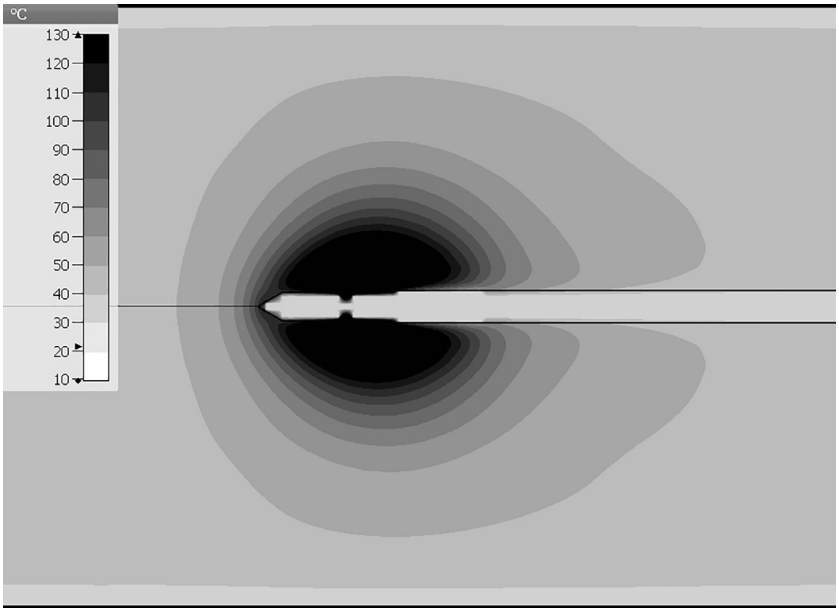

Fig. 8. Representation of the calculated temperature distribution of the coaxial slot antenna at a microwave power of 90 W and a flow coefficient of 60,000 W/(K*m³) after 10 min. The extension of the temperature distribution over time reaches the following dimensions: 24.9 mm/19.3 mm (width/length) after 30 s, 31.9 mm/28.5 mm after 90 s, 36.1 mm/33.0 mm after 300 s and 36.1 mm/33.1 mm after 600 s regarding the 50 °C zone; 22.9 mm/16.2 mm after 30 s, 27.1 mm/24.4 mm after 90 s, 29.8 mm/27.9 mm after 300 s and 29.8 mm/28.0 mm after 600 s regarding the 60 °C zone.

between coagulated tissue and tissue located in the transition zone without contrast agent in an ex vivo sample [27]. At temperatures lower than 60 °C for an extended period of time, coagulation of the tissue may also be achieved (e.g., temperatures of 50–52 °C induce cytotoxicity over 4–6 min) [1]. Between 60° and 100 °C, near instantaneous induction of protein coagulation occurs [1,28]. For clinical application (e.g., in MR- and CT-based thermometry), the time point of the instantaneous induction of coagulation is relevant to minimize patient treatment time while being sure to have completely destroyed the lesion. When the periphery of the treating zone is considered as coagulated, the ablation will be stopped to protect surrounding healthy tissue. Therefore, the evaluation is based on the 60 °C isothermal area.

One of the reasons of the difference in results between the area evaluation and the Bland–Altman analysis can be resulted from the fact that the 60 °C isothermal area, in which the tissue is almost immediately destroyed, does not correspond to the actual ablation zone. In the simulation, the ablation zone should not depend on a certain temperature value, but should be time-dependent at certain temperatures. As described above, even at lower temperatures over a certain period of time, proteins can already denature, so that the simulated ablation zones should be larger and should shift the comparison of the ablation zones to higher flow coefficients.

Furthermore, the simulation does not consider the deviating heat loss in the peripheral liver (outside the heating area). Although the heat transfer is lower in this area and it could affect the size of the ablation zone. More complex models could further improve the results. Other solutions for calculating the temperature distribution in a microwave ablation in ex vivo liver tissue could be a two-compartment model of the liver (two different local flow coefficients) or a nonlinear flow coefficient. These would also describe the peripheral areas of the ablation zone in the liver mathematically.

Another approach could be to preheat the liver sample in saline solution to 37 °C to limit dehydration of the liver tissue and fill the empty blood vessels of the ex vivo sample. The initial temperatures would also be closer to the clinical (intraoperative) conditions. Since in the literature the ex vivo evaluations of microwave antennas and tissue properties are often realized at room temperatures [7,8,10], a water bath was not considered in this study as well. Since the liver tissue was received freshly from the slaughterhouse, there should be no limitations due to dehydration. Furthermore, as this study examines only the ex vivo properties of the liver sample in terms of the heat transfer, an in vivo similar condition was not required.

In summary, the evaluation of the ablation zones resulted in an optimal flow coefficient of 50,000 W/(K*m^3) for simulation of the microwave ablation in ex vivo liver samples, but some sources of errors in the evaluation should be considered. On the other hand, the presented model in the current paper shows optimal results between the accurately measured temperature values from the experiments and the simulation with a flow coefficient of 90,000 W/(K*m^3) and power levels greater than 60 W. Developed microwave applicator systems can be evaluated with this model for ex vivo liver tissue.

5. Conclusion

In this work, a validation of a microwave thermal ablation simulation in ex vivo porcine liver at different flow coefficients was performed. To assess the simulation model, liver tissue was heated with a commercially available ablation system and temperatures were recorded simultaneously at multiple positions. Additionally, MR imaging was performed after heating and the ablation zone observed on the images was compared to the calculated heat distribution. The evaluation of the areas resulted in an optimal flow coefficient of 50,000 W/(K*m^3). However, this method includes some systematic errors. In contrast, the Bland–Altman analysis showed a significant agreement of the measured temperatures with the simulated temperatures at a flow coefficient of 90,000 W/(K*m^3).

Competing interests

None declared.

Funding

This research was supported by the German Research Foundation (Deutsche Forschungsgemeinschaft, DFG) in the context of the priority program ESSENCE, with the reference numbers VO 479/17-1 and JA 921/52-1, to the institute IDIR of the J.W. Goethe-University of Frankfurt and the Technical University of Darmstadt, respectively.

Ethical approval

Not required.

References

[1] Goldberg SN, Gazelle GS, Mueller PR. Thermal ablation therapy for focal malignancy: a unified approach to underlying principles, techniques, and diagnostic imaging guidance. AJR Am J Roentgenol 2000;174(2):323–31.
[2] Vogl TJ, Nour-Eldin NA, Hammerstingl RM, Panahi B, Naguib NNN. Microwave Ablation (MWA): basics, technique and results in primary and metastatic liver neoplasms – review article. Rofo 2017;189(11):1055–66.
[3] Tabuse K, Katsumi M, Kobayashi Y, Noguchi H, Egawa H, Aoyama O, Kim H, Nagai Y, Yamaue H, Mori K, et al. Microwave surgery: hepatectomy using a microwave tissue coagulator. World J Surg 1985;9(1):136–43.
[4] Kaltenbach B, Roman A, Eichler K, Nour-Eldin NE, Vogl TJ, Zangos S. Real-time qualitative MR monitoring of microwave ablation in ex vivo livers. Int J Hyperthermia 2016;32(7):757–64.
[5] Prakash P. Theoretical modeling for hepatic microwave ablation. Open Biomed Eng J 2010;4:27–38.
[6] Rubio MF, Hernández AV, Salas LL, Ávila-Navarro E, Navarro EA. Coaxial slot antenna design for microwave hyperthermia using finite-difference time-domain and finite element method. Open Nanomed J 2011;3:2–9.
[7] Brace CL. Dual-slot antennas for microwave tissue heating: parametric design analysis and experimental validation. Med Phys 2011;38(7):4232–40.
[8] Chiang J, Hynes KA, Bedoya M, Brace CL. A dual-slot microwave antenna for more spherical ablation zones: ex vivo and in vivo validation. Radiology Aug 2013;268(2):382–9.
[9] Zurbuchen U, Holmer C, Lehmann KS, Stein T, Roggan A, Seifarth C, Buhr HJ, Ritz JP. Determination of the temperature-dependent electric conductivity of liver tissue ex vivo and in vivo: importance for therapy planning for the radiofrequency ablation of liver tumours. Int J Hyperthermia 2010;26(1):26–33.
[10] Lopresto V, Pinto R, Lovisolo GA, Cavagnaro M. Changes in the dielectric properties of ex vivo bovine liver during microwave thermal ablation at 2.45GHz. Phys Med Biol 2012;57(8):2309–27.
[11] Gas P. Multi–frequency analysis for interstitial microwave hyperthermia using multi-slot coaxial antenna. J Electr Eng 2015;66(1):26–33.
[12] Rattanadecho P, Keangin P. Numerical study of heat transfer and blood flow in two-layered porous liver tissue during microwave ablation process using single and double slot antenna. Int J Heat Mass Transf 2013;58(1):457–70.
[13] Giavarina D. Understanding Bland Altman analysis. Biochem Med (Zagreb) 2015;25(2):141–51.
[14] Rossmann C, Garrett-Mayer E, Rattay F, Haemmerich D. Dynamics of tissue shrinkage during ablative temperature exposures. Physiol Meas 2014;35(1):55–67.
[15] Park CS, Hall SK, Liu C, Payne SJ. A model of tissue contraction during thermal ablation. Physiol Meas 2016;37(9):1474–84.
[16] Liu D, Brace CL. Numerical simulation of microwave ablation incorporating tissue contraction based on thermal dose. Phys Med Biol 2017;62(6):2070–86.
[17] Lopresto V, Pinto R, Farina L, Cavagnaro M. Treatment planning in microwave thermal ablation: clinical gaps and recent research advances. Int J Hyperthermia Feb 2017;33(1):83–100.
[18] Lazebnik M, Converse MC, Booske JH, Hagness SC. Ultrawideband temperature-dependent dielectric properties of animal liver tissue in the microwave frequency range. Phys Med Biol 2006;51(7):1941–55.
[19] Reimann C, Puentes M, Maasch M, Hübner F, Bazrafshan B, Vogl TJ, Damm C, Jakoby R. Planar microwave sensor for theranostic therapy of organic tissue based on oval split ring resonators. Sensors (Basel) 2016;16(9).
[20] Brace CL, Diaz TA, Hinshaw JL, Lee FT Jr. Tissue contraction caused by radiofrequency and microwave ablation: a laboratory study in liver and lung. J Vasc Interv Radiol 2010;21(8):1280–6.

[21] Farina L, Weiss N, Nissenbaum Y, Cavagnaro M, Lopresto V, Pinto R, Tosoratti N, Amabile C, Cassarino S, Goldberg SN. Characterisation of tissue shrinkage during microwave thermal ablation. Int J Hyperthermia 2014;30(7):419–28.
[22] Amabile C, Farina L, Lopresto V, Pinto R, Cassarino S, Tosoratti N, Goldberg SN, Cavagnaro M. Tissue shrinkage in microwave ablation of liver: an ex vivo predictive model. Int J Hyperthermia 2017;33(1):101–9.
[23] Liu D, Brace CL. CT imaging during microwave ablation: analysis of spatial and temporal tissue contraction. Med Phys 2014;41(11):113303.
[24] Alonzo M, Bos A, Bennett S, Ferral H. The emprint™ ablation system with thermosphere™ technology: one of the newer next-generation microwave ablation technologies. Semin Intervent Radiol 2015;32(4):335–8.
[25] Vogl TJ, Roman A, Nour-Eldin NA, Hohenforst-Schmidt W, Bednarova I, Kaltenbach B. A comparison between 915MHz and 2450MHz microwave ablation systems for the treatment of small diameter lung metastases. Diagn Interv Radiol 2018;24(1):31–7.
[26] Vogl TJ, Hagar A, Nour-Eldin NA, Gruber-Rouh T, Eichler K, Ackermann H, Bechstein WO, Naguib NN. High-frequency versus low-frequency microwave ablation in malignant liver tumours: evaluation of local tumour control and survival. Int J Hyperthermia 2016;32(8):868–75.
[27] Vogl TJ, Basten LM, Nour-Eldin NA, Kaltenbach B, Bodelle B, Wichmann JL, Ackermann H, Naguib NNN. Evaluation of microwave ablation of liver malignancy with enabled constant spatial energy control to achieve a predictable spherical ablation zone. Int J Hyperthermia 2018;34(4):492–500.
[28] Vogl TJ, Naguib NN, Lehnert T, Nour-Eldin NE. Radiofrequency, microwave and laser ablation of pulmonary neoplasms: clinical studies and technical considerations – review article. Eur J Radiol 2011;77(2):346–57.